



Influence of arc energy and filler metal composition on the microstructure in wire arc additive manufacturing of duplex stainless steels

Benjamin Wittig¹ · Manuela Zinke¹ · Sven Jüttner¹

Received: 22 July 2020 / Accepted: 14 September 2020 / Published online: 28 September 2020
© The Author(s) 2020

Abstract

The influence of arc energy and filler metal composition on the microstructure of additively welded thin-walled structures of duplex stainless steels was investigated using different commercially available standard and superduplex solid wire electrodes commonly used today. As welding process, the cold metal transfer (CMT) process was used. The arc energy and cooling rate were varied by adjusting the wire feed and welding speed. Optical emission spectroscopy (OES) and carrier gas melt extraction (CGME) were used to determine the chemical composition of the specimens. The ferrite content was determined both by magnetic induction and by image analysis as a function of the wall height. In addition, the microsections were examined for intermetallic phases and precipitations. Moreover, corrosion tests were carried out according to ASTM G 48, Method A. The results indicate that an increase in arc energy leads to longer $t_{12/8}$ cooling times. Depending on the filler metal composition, this leads to ferrite contents that are partially outside the values required according to ISO 17781. Furthermore, precipitates of secondary austenite are often found, which is attributed to the multiple reheating by the subsequent layers.

Keywords Duplex stainless steels · Additive manufacturing · Ferrite content · Secondary phases · Thermal cycles · CMT

1 Introduction

Currently, wire arc additive manufacturing (WAAM) is gaining enormous importance. Especially in the processing of high-alloyed, expensive materials, the production of near net shape objects by means of layer-by-layer deposition welding offers considerable advantages, e.g., the ability to produce complex geometric shape elements with a high degree of material utilization [1–3]. However, a challenge in additive arc welding is the relatively high heat input coupled with relatively low heat dissipation. This can lead to residual stresses and distortion as

well as to changes in the microstructure and crack formation [4, 5]. This becomes particularly critical in the processing of materials that already require demanding handling from a welding point of view. Especially, the welding of duplex stainless steels requires an adjusted heat control to achieve material-specific properties in the weld metal. Current recommendations for welding duplex stainless steels focus on achieving a precipitation-free weld metal microstructure with balanced proportions of ferrite and austenite during joint welding and cladding [6, 7]. However, the application of these recommendations regarding arc energy and filler metals result in a predominantly austenitic microstructure in WAAM of duplex stainless steel components [8]. Reasons for the excessive precipitation of austenite, especially in thin-walled structures, are the increasing cooling time with increasing wall height as well as the repeated dwell time in the temperature range of 1200–800 °C when welding the subsequent layers [9, 10].

Since there are no reliable recommendations for the WAAM of duplex stainless steels, the objective of this study was to evaluate the influence of arc energy and filler metal composition on the microstructure of additively

Recommended for publication by Commission II - Arc Welding and Filler Metals

✉ Benjamin Wittig
benjamin.wittig@ovgu.de

¹ Institute of Materials and Joining Technology, Otto von Guericke University, Magdeburg, Germany

welded thin-walled structures of duplex stainless steels. The focus was not only on the ferrite-austenite ratio itself but also on the potential precipitation of secondary phases, such as secondary austenite.

2 Experimental

2.1 Filler metals and shielding gases

Filler metals for this study included different commercially available standard and superduplex solid wire electrodes with a diameter of 1.2 mm. The wire batch of the G Z 22 8 3 L Si was also provided with a diameter of 1.0 mm. Table 1 shows the chemical composition of the filler metals that was determined on button melts produced in an arc melter under pure argon atmosphere (99.996 %).

Based on the chemical composition of the filler metals, the expected ferrite number (FN) as a measure of the ferrite content can be estimated using the WRC-1992 diagram [11]. Table 2 shows the chromium (Eq. 1) and nickel (Eq. 2) equivalents calculated for the filler metals, which can be used to determine the FN in the WRC-1992 diagram:

$$Cr_{Eq} = Cr + Mo + 0.7Nb \quad (1)$$

$$Ni_{Eq} = Ni + 35C + 20N + 0.25Cu \quad (2)$$

Shielding gases for the additive CMT welds included an active gas mixture (Ar + 30 % He + 2 % CO₂) that was used for the standard duplex wires as well as an inert gas mixture (Ar + 30 % He) that was selected for the superduplex wires, since previous investigations by Stützer et al. [12] have shown that even very low amounts of CO₂ in the shielding gas can lead to pores in superduplex weld metal.

2.2 WAAM setup

The layer-by-layer technique in combination with the GMAW-CMT process was used to produce wall structures of 20 layers with a length of 200 mm (Fig. 1). The deposition

Table 2 Chromium and nickel equivalents as well as ferrite numbers (FN) of the filler metals according to the WRC-1992 diagram

Filler metal	Cr _{Eq}	Ni _{Eq}	FN
Standard duplex			
G 22 9 3 N L	26.0	12.2	54
G Z 22 8 3 L Si	26.3	12.2	57.5
G Z 22 5 3 L	25.4	9.0	> 100
Superduplex			
G 25 9 4 N L	29.8	14.6	63
G Z 25 10 4 L	29.1	15.4	47
G Z 29 8 2 L	30.9	15.1	67

welds were performed with a neutral torch position, a contact tip to work distance of 12 mm, and a shielding gas flow rate of 18 l/min. The single layers were welded in PA (1G) position with alternating welding direction.

To evaluate the influence of the arc energy, the wire feed speed (i.e., welding current) and the travel speed were varied in the ranges given in Table 3. During the production of the wall structures, the welding parameters for the respective walls were kept constant over all layers. The welding parameters were recorded and evaluated by means of the internal documentation function of the welding power source. An external data logging system was also used for verification. The t_{12/8} cooling time was measured for each layer using a pyrometer. In addition, thermocouples were attached between the 3rd and 4th layer after welding the 4th layer and between the 10th and 11th layer after welding the 11th layer to record the temperature cycles for determining the dwell times in the temperature ranges that are relevant for adverse precipitations.

2.3 Characterization methods

The geometries of the welded wall structures were measured regarding their thickness and height. The ferrite content was determined in the bottom, middle, and top of the walls on cross-sections both by magnetic induction using a Fischer Feritscope® and by image analysis using micrographs. In addition, the microstructure was analyzed with regard to the

Table 1 Chemical composition (wt.%) of the filler metals determined by OES and CGME* (filler metal designation acc. ISO 14343-A)

Filler metal	C*	Si	Mn	Cr	Ni	Mo	Cu	W	N*	PREN
Standard duplex (30 ≤ PREN < 40)										
G 22 9 3 N L	0.012	0.52	1.57	22.9	8.54	3.11	0.05	< 0.01	0.16	35.7
G Z 22 8 3 L Si	0.012	0.77	1.58	23.2	8.56	3.11	0.09	< 0.01	0.16	36.0
G Z 22 5 3 L	0.019	0.45	0.75	22.1	5.51	3.22	0.18	0.025	0.14	35.0
Superduplex (PREN ≥ 40)										
G 25 9 4 N L	0.016	0.35	0.84	25.7	9.04	4.17	0.53	0.53	0.24	43.3
G Z 25 10 4 L	0.015	0.42	0.37	25.2	9.49	3.95	0.09	< 0.01	0.27	42.5
G Z 29 8 2 L	0.024	0.39	1.01	28.7	6.94	2.19	0.14	< 0.01	0.36	41.7

$$PREN = Cr + 3.3Mo + 16N \quad [14]$$

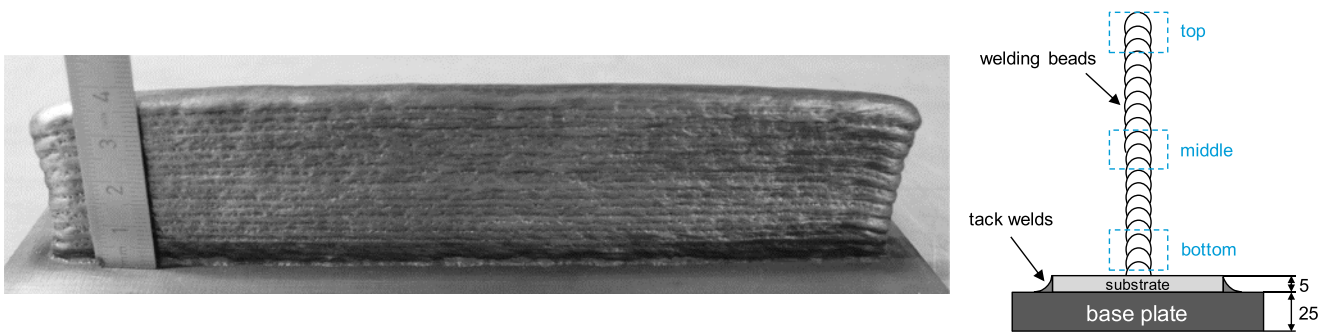


Fig. 1 Specimen geometry and indication of the areas of analysis

occurrence of precipitations and inclusions. For the determination of the ferrite-austenite ratio by image analysis, the samples were etched using Beraha II to obtain sufficiently high contrasts. Oxalic acid and NaOH were used in addition to examine the presence of precipitations. Optical emission spectroscopy (OES) and carrier gas melt extraction (CGME) were used to determine the chemical composition of the walls and to evaluate pickup or burning loss of alloying elements. To prove the corrosion resistance of the walls, the ferric chloride pitting test was carried out according to ASTM G48, Method A [13]. Before testing, all surfaces of the specimens were milled and then polished using 120-grit abrasive paper. In accordance with ISO17781:2017 [14], the corrosion test was carried out in as-welded condition at a test temperature of 22 °C for the standard duplex specimens and 35 °C for the superduplex specimens. The acceptance criterion is a weight loss < 4 g/m².

3 Results and discussion

3.1 Effect of welding parameters on wall geometry

For the experiments on the influence of the arc energy, both the wire feed speed (v_{WFS}) and the travel speed (v_{TS}) were varied in several steps. Since the control characteristic of the

Table 3 Overview of the process parameters for the production of the wall structures

Parameter	Setting
Welding process	GMAW-CMT
Welding position	PA (1G)
Welding torch angle	$\alpha = 0^\circ, \beta = 0^\circ$
Shielding gas flow rate	18 l/min
Contact tip to work distance	12 mm
Wire feed speed (v_{WFS})	4–7 m/min
Travel speed (v_{TS})	0.3–0.7 m/min
Arc energy (E)	0.09–0.66 kJ/mm
Interpass temperature (T_{IP})	≤ 100 °C

welding power source has sometimes led to considerable deviations (up to 0.7 m/min) between set and real wire feed speed, the measured mean values are used in this paper. As can be seen in Fig. 2a, both the travel speed and the wire feed speed directly influence the geometry of the walls. With constant travel speed and increasing wire feed speed (i.e., increasing arc energy), the wall thickness and height increase due to the increasing deposition rate. The change in travel speed also influences the wall thickness as well as the wall height at constant wire feed speed (i.e., constant deposition rate). Both wall thickness and height decrease with increasing travel speed (i.e., decreasing arc energy). This allows varying the wall thickness and height via the v_{WFS}/v_{TS} ratio at constant deposition rates. Thus, a specific adjustment of the wall thickness of WAAM components is possible by selecting the welding parameters. However, an increase of the seam cross-section is always coupled with an increase of the arc energy and thus with a higher heat input, which can have a negative effect on the ferrite-austenite ratio. Figure 2b compares the cross-sections of different walls. As can be seen here, not only the seam cross-section increases with increasing arc energy but also the waviness of the specimen surface increases, which can lead to major post-processing depending on the requirements of the final component.

3.2 Effect of arc energy on $t_{12/8}$ cooling time and temperature cycle

By increasing the arc energy, the seam cross-section can be increased, and thus, the number of necessary beads for the required final geometry can be reduced. However, this is coupled with an increased heat input, which results in slower cooling rates. The correlation between arc energy and $t_{12/8}$ cooling time is shown in Fig. 3a as an example for different arc energies. On the one hand, the results show that an increase in arc energy leads to significantly higher $t_{12/8}$ cooling times in the respective layers. On the other hand, it can be seen that the $t_{12/8}$ cooling times stabilize on a certain level from about the 4th–5th layer. This indicates that above this layer height, there is only a two-dimensional heat dissipation (along and perpendicular to the welding direction), and the base material is of

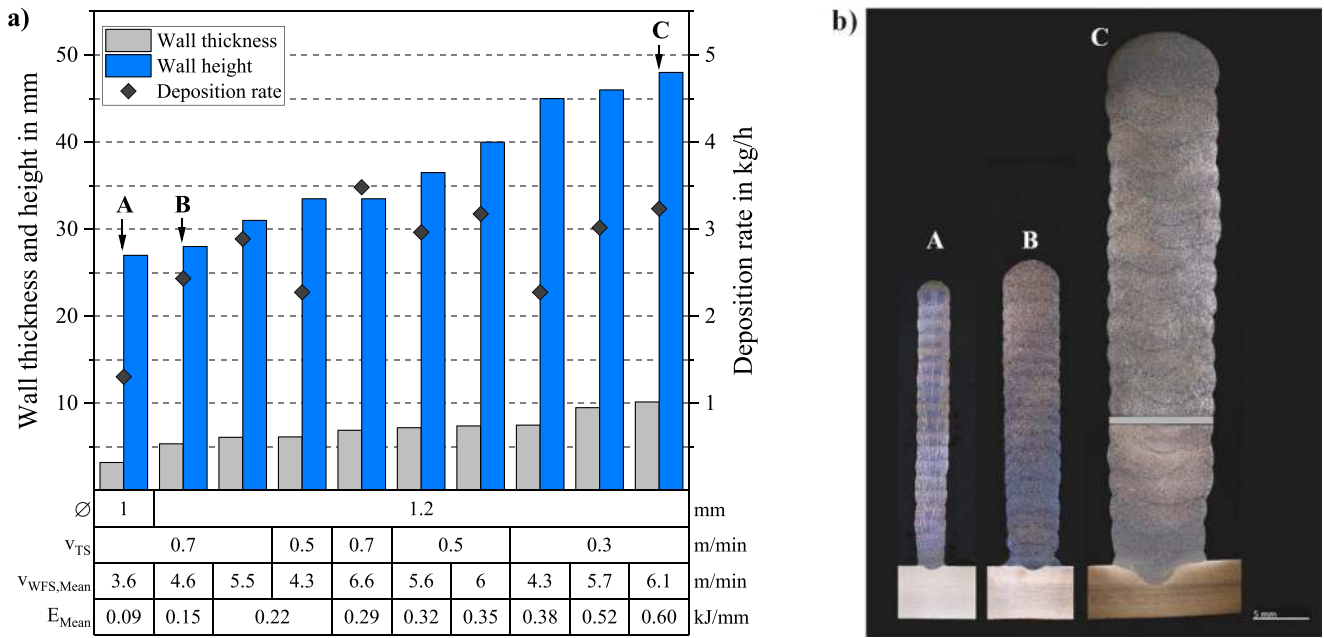


Fig. 2 a Influence of the welding parameters on wall geometry and deposition rate. b Cross-sections of representative specimens consisting of 20 layers each

minor importance for heat dissipation. This leads to significantly longer cooling times compared with joint welding, as can be seen from the reference lines. These were determined at the research facility during joint welding of superduplex stainless steel using pulsed arc. The $t_{12/8}$ cooling times ranged between 1.8 and 3.2 s, and the arc energy was 0.7–0.8 kJ/mm. Due to the surrounding base material and filler beads, the heat is dissipated much faster despite higher arc energies. This relationship is shown schematically in Fig. 3b.

A similar effect can be observed with the dwell times in high temperature ranges. Due to the welding of the next layers, the lower layers are repeatedly heated and pass through temperature ranges where critical phase precipitations, such as sigma phase (σ), secondary austenite (γ_2), carbides, or nitrides, can form (Fig. 4). With increasing arc energy, the peak temperatures and dwell times in the reheated layers also increase. This indicates an elevated risk of adverse phase precipitations with increasing arc energy.

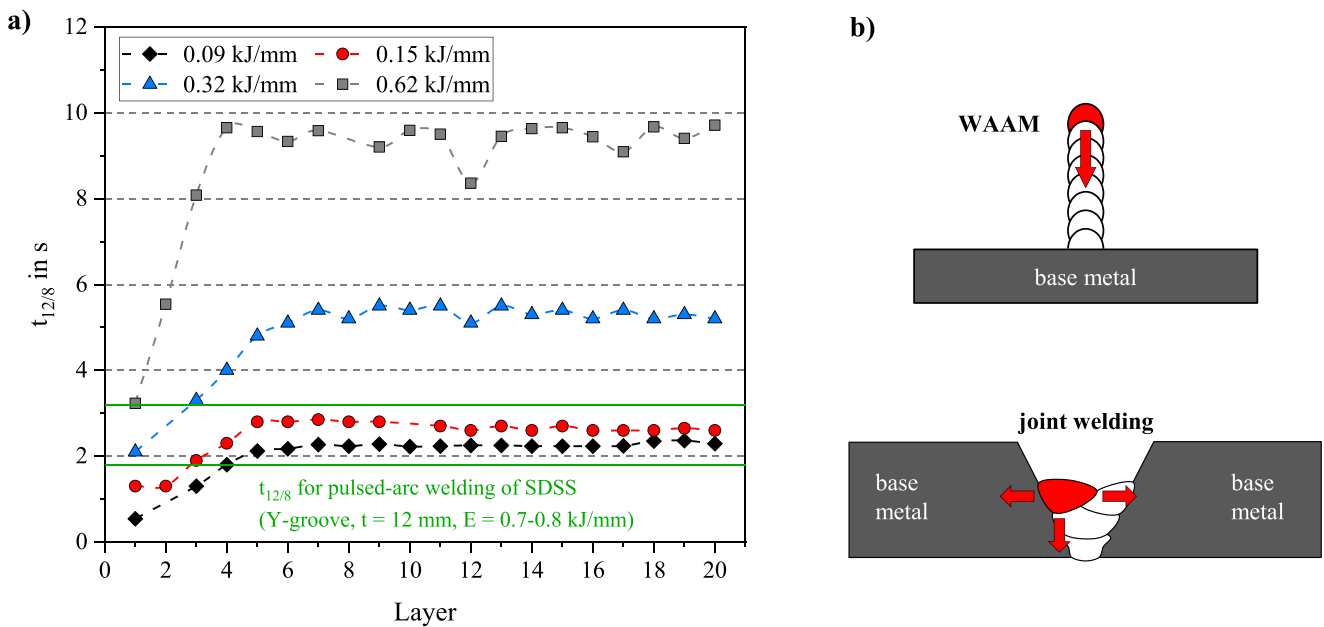
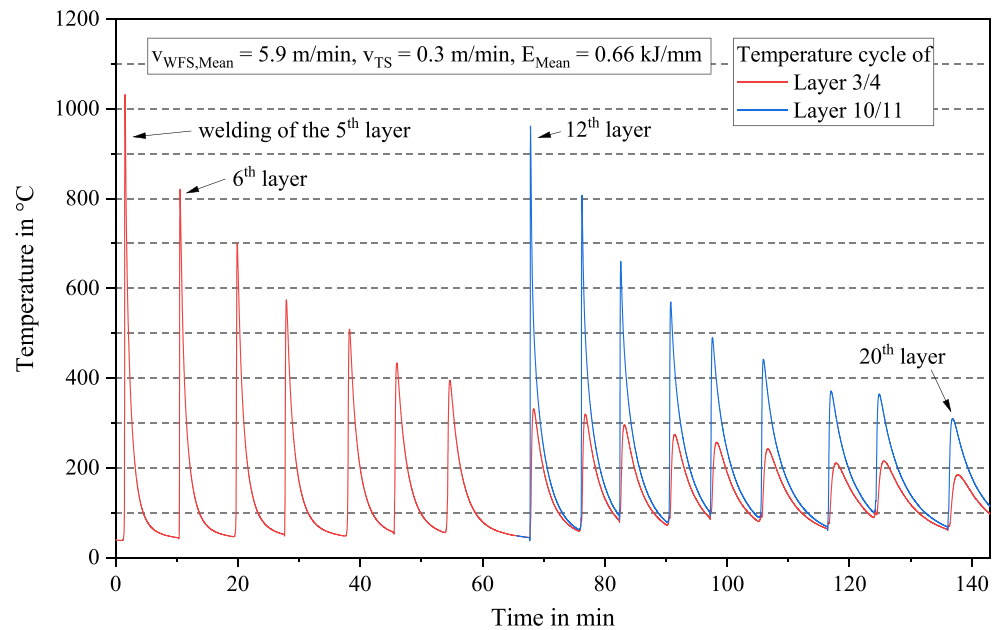


Fig. 3 a Comparison of the $t_{12/8}$ cooling times of WAAM walls as a function of arc energy and layer. b Schematic comparison of heat dissipation between WAAM and joint welding

Fig. 4 Exemplary temperature cycle of a WAAM wall



3.3 Effect of arc energy on microstructure

The metallographic investigations show that the ferrite-austenite ratio is partly subject to strong fluctuations. Thus, it may happen that there is much less austenite at the fusion lines between the beads than within the beads, which is due to reheating by the subsequent layers (Fig. 5). These inhomogeneities in the microstructure complicate the determination of the ferrite content using image analysis. Image analysis requires images with sufficiently high magnification and resolution to allow a proper separation of the microstructures.

Because there are partly significant differences in the microstructure proportions in neighboring areas, the result strongly depends on where and how many images are taken by the operator. In the example in Fig. 5, there is a difference in the ferrite content of 20 %. In order to reduce the risk of biased results due to these influences, the images for image analysis and ferrite content determination were taken using a digital microscope. This enables panoramic images in $\times 500$ magnification with up to 100 stitched single images. Thus, a large region of interest can be analyzed at once, and a reliable mean value for the ferrite content can be determined (Fig. 6). This

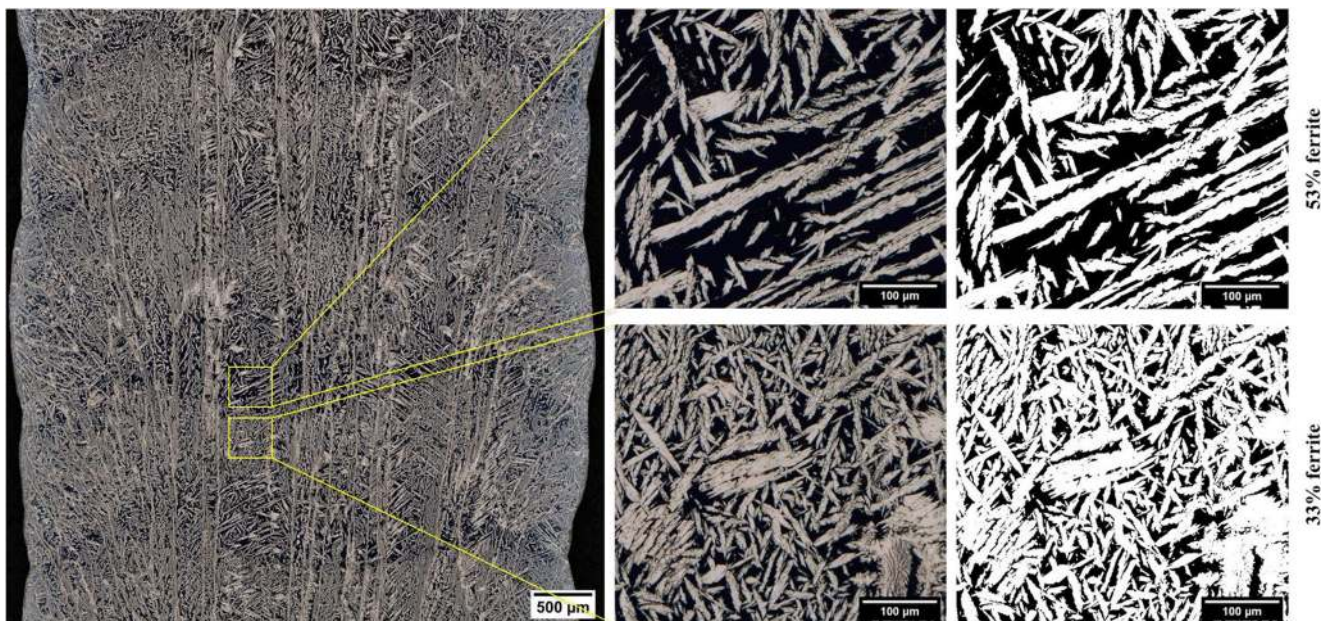


Fig. 5 Microstructure of an exemplary WAAM wall of G 22 9 3 N L and binary image analysis for determining the ferrite content using single images. Etching: Beraha II. Austenite = light, Ferrite = dark

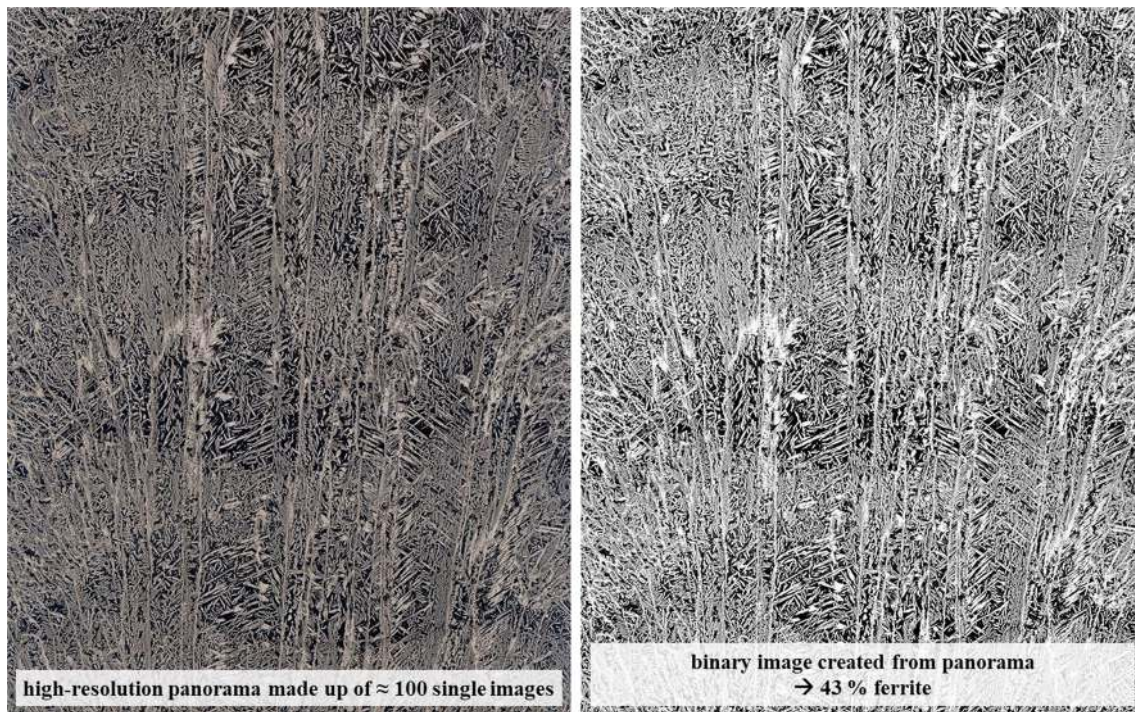


Fig. 6 Binary image analysis for determining the ferrite content using panoramas. Ferrite = black, austenite = white

was done in three different positions in the cross-section (bottom, middle, top) and at two cross-sections for each wall.

The results of the ferrite determination by Feritscope® (in FN) and image analysis (in %) as a function of arc energy and area of analysis are shown in Fig. 7 using the example of the G 22 9 3 N L and G Z 22 8 3 L Si. As can be seen, the FN and the ferrite percent show basically the same tendencies with regard to the influence of the arc energy. An increase in the arc energy obviously leads to lower ferrite contents. This is due to the cooling times and temperature cycles described above, which are significantly influenced by the arc energy.

When looking at the results with regard to the area of analysis, it is obvious that the FN and the ferrite percent also show mostly the same tendencies, but in some cases, there are contrary tendencies. However, the majority of the results indicate that the ferrite content is higher in the upper layers than in the middle and lower layers. One possible reason for this is that the 18th–20th layers were included in the analysis of the upper layers. The 19th layer experienced only one and the 20th layer no reheating by subsequent layers into temperature ranges that are relevant for austenite precipitation, so that the ferrite content here is higher than in the layers below. Furthermore, it is

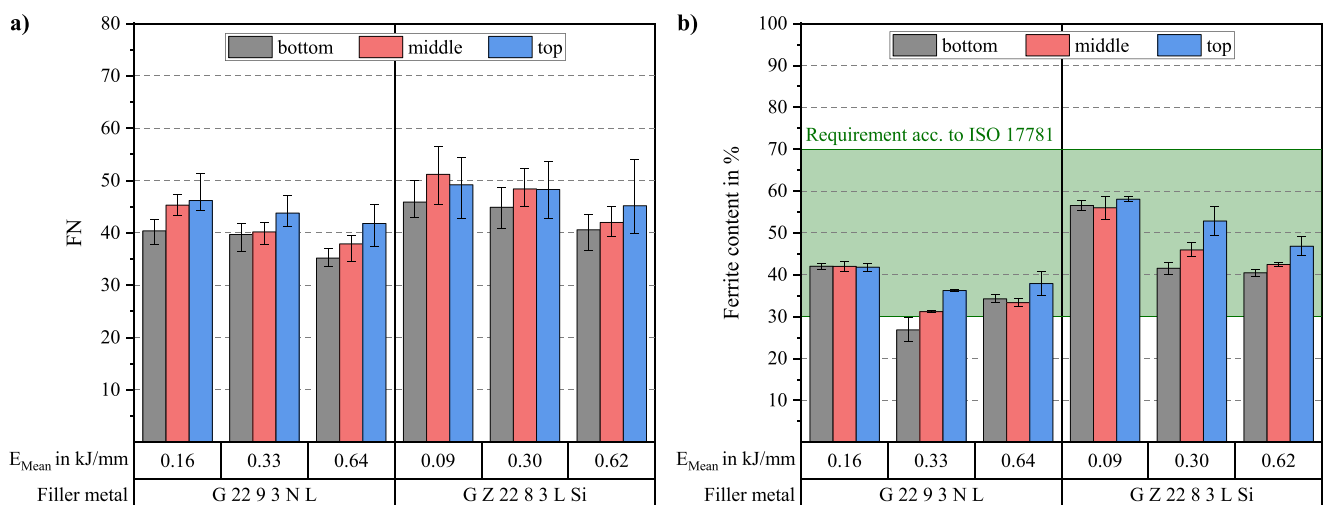


Fig. 7 Results of ferrite content determination using Feritscope® (in FN) and image analysis (in %) as a function of arc energy and area of analysis using the example of G 22 9 3 N L and G Z 22 8 3 L Si

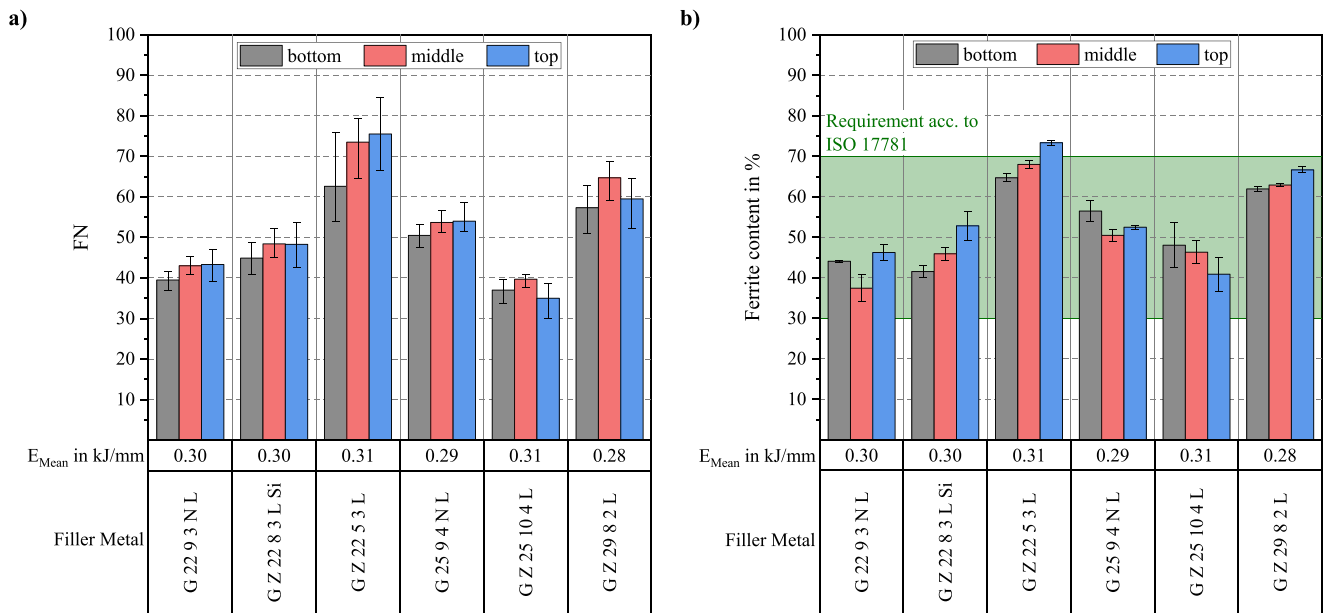


Fig. 8 Results of ferrite content determination using Feritscope® (in FN) and image analysis (in %) as a function of filler metal composition and area of analysis at comparable arc energies

evident that ferrite percent contents may be obtained which do not meet the requirements of ISO17781 [14]. For example, in the case of the G 22 9 3 N L, it is to be expected that unacceptably high austenite contents will occur at arc energies above 0.3 kJ/mm. In contrast to that, the G Z 22 8 3 L Si seems to provide an acceptable ferrite-austenite ratio over a wide range of different arc energies.

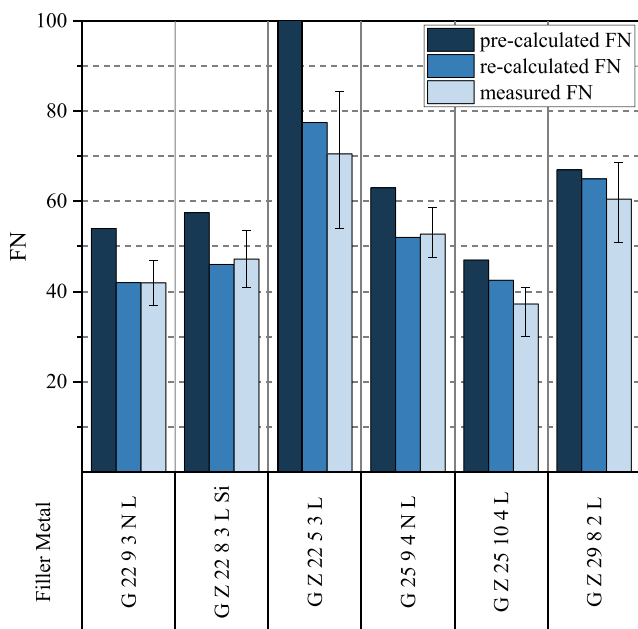


Fig. 9 Comparison of pre-calculated vs. re-calculated vs. measured FN

3.4 Effect of filler metal composition on microstructure

To determine the influence of the filler metal composition on the ferrite-austenite ratio, walls were produced with different filler metals (cf. Table 1) but same welding parameters. Due to the previously described control characteristic of the welding power source, the actual values of the different walls differ slightly, but the arc energies are at a comparable level. Figure 8 shows the influence of the filler metal composition on the ferrite content (in FN and %). As can be seen, the FN and the ferrite percent basically reflect the same trends with regard to the influence of the filler metal composition. For example, it is apparent that the highest ferrite contents in the wall structures can be achieved with the nickel-reduced G Z 22 5 3 L and the higher chromium-alloyed G Z 29 8 2 L. In the case of the

Table 4 Chemical composition (wt.%) of the WAAM walls determined by OES and CGME* (short overview of alloying elements affected by pickup and burning loss)

Filler metal	C*	ΔC	Cr	ΔCr	N*	ΔN
G Z 22 9 3 N L	0.020	+ 0.008	22.5	- 0.37	0.16	+ 0.0032
G Z 22 8 3 L Si	0.015	+ 0.004	22.7	- 0.33	0.16	+ 0.0039
G Z 22 5 3 L	0.023	+ 0.004	21.9	- 0.24	0.19	+ 0.0516
G Z 25 9 4 N L	0.014	- 0.002	24.9	- 0.73	0.23	- 0.0106
G Z 25 10 4 L	0.014	- 0.001	24.5	- 0.63	0.27	- 0.0013
G Z 29 8 2 L	0.023	- 0.001	28.2	- 0.46	0.35	- 0.0173

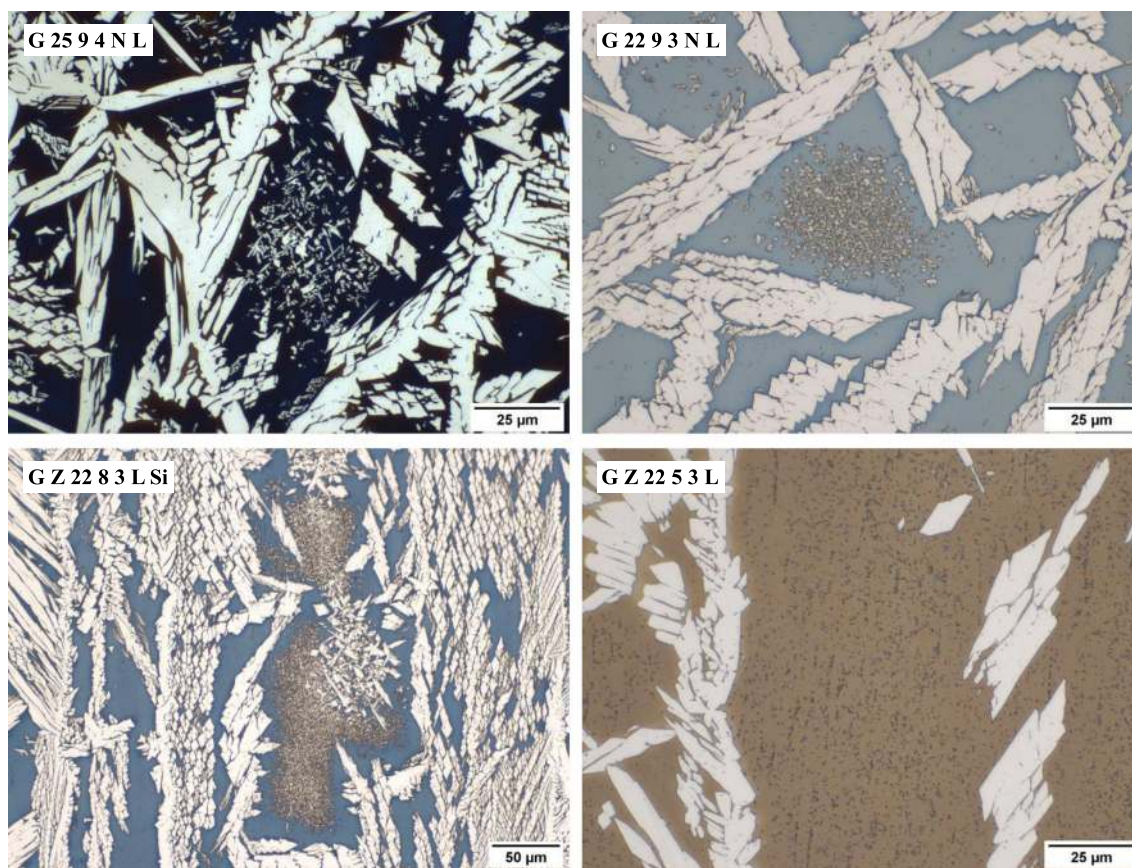


Fig. 10 Presence of secondary austenite and nitrides in WAAM walls of different filler metal compositions; etching: Beraha II

G Z 22 5 3 L, the ferrite content may even become unacceptably high. In contrast, significantly lower ferrite contents are achieved with the standard duplex filler metal G 22 9 3 N L.

In principle, the influence of the filler metal composition can also be estimated using the WRC-1992 diagram. However, this requires knowledge of the exact chemical composition of the weld metal. Otherwise, relatively strong deviations may occur, as illustrated in Fig. 9. Here, the measured FN is compared with the pre-calculated FN (based on the chemical composition of the filler metals) and the re-calculated FN (based on the chemical composition of the weld metal). A major reason for the deviations between pre-calculated and measured FN is the pickup and burning loss of alloying elements during welding. For example, a significant pickup of nitrogen (+ 516 ppm) was detected in the wall of G Z 22 5 3 L (Table 4). Furthermore, a slight to moderate burning loss of chromium was determined for all filler metals. Since these elements are included in the calculation of the chromium and nickel equivalents (cf. Eqs. 1 and 2), the prediction is subject to inaccuracies. However, if the chemical compositions of the walls are then used to predict the FN values (re-calculated FN), taking into account the pickups and burning losses, it can be seen that the predicted and measured FN values are very close to each other.

The metallographic examination with regard to the presence of unwanted phase precipitations shows that secondary austenite (γ_2) is often formed. A specific quantification of the γ_2 contents is not possible on the basis of the micrographs. However, from a qualitative point of view, the quantity of γ_2 depends mainly on the filler metal composition and to a minor extent on the arc energy. γ_2 was found in all specimens, with the exception of the walls made of G Z 25 10 4 L and G Z 29 8 2 L, in which at most, a beginning γ_2 formation at very few spots can be suspected. Sporadic indications of γ_2 were identified in the specimens of G Z 22 5 3 L, while larger amounts of γ_2 were detected in the specimens of G 25 9 4 N L and G 22 9 3 N L (Fig. 10). A particularly strong γ_2 formation was found in the WAAM walls of G Z 22 8 3 L Si (Fig. 10). A possible reason for the strong γ_2 formation in the G Z 22 8 3 L Si is the increased silicon content compared with the other filler metals (cf. Table 1). When comparing the specimens of G Z 25 10 4 L and G 25 9 4 N L, there is a significant difference in the tungsten content. While the G Z 25 10 4 L does not contain any quantifiable tungsten, the more γ_2 susceptible G 25 9 4 N L contains significantly more tungsten with 0.53 wt.%. Both silicon and tungsten shift the precipitation of γ_2 to shorter times [16]. In the last welded layer (20th layer), no γ_2 was found in any of the WAAM walls, which suggests that γ_2 is in fact only caused by the reheating from the subsequent layers.

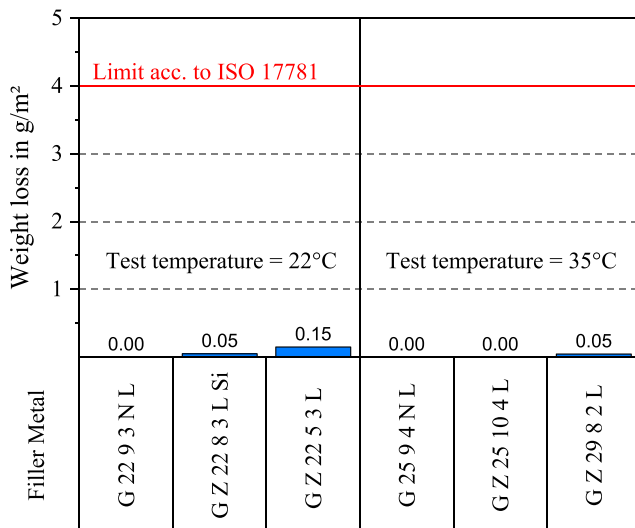


Fig. 11 Results of the ferric chloride pitting corrosion test according to ASTM G48, Method A

In the wall structures of G Z 22 5 3 L, fine nitride precipitations were also found in addition to γ_2 . This is because of the low solubility of nitrogen in the ferrite in combination with the high ferrite content in the wall of the G Z 22 5 3 L. Thus, the excess nitrogen cannot diffuse into the austenite [17]. Evidence of intermetallic phases, such as σ phase, could not be found in any of the walls, which is in good agreement with simulations made by Hosseini et al. [15].

3.5 Corrosion behavior

In the literature, both secondary austenite and nitrides are often described as detrimental with regard to corrosion resistance [18–20]. However, in the present investigations, no significant corrosion phenomena can be detected under the required test conditions with the ferric chloride pitting test according to ASTM G48, Method A. As the results in Fig. 11 show, there is no significant weight loss in any of the specimens. There is also no visual evidence of pitting.

4 Conclusions

The influence of arc energy and filler metal composition on the microstructure of additively welded thin-walled structures of duplex stainless steels was investigated. The arc energy was varied between 0.09 and 0.66 kJ/mm using the CMT process. Three different standard duplex and three different superduplex filler metals were used to evaluate the influence of the chemical composition. The following conclusions can be drawn:

- 1 The wall thickness of WAAM components can be varied via the v_{WFS}/v_{TS} ratio when using GMAW processes.

Thus, an increase in the seam cross-section leads to an increase in arc energy.

- 2 The $t_{12/8}$ cooling times and dwell times in high temperature ranges increase significantly with an increase in arc energy. Furthermore, the cooling time extends with increasing wall height (number of layers) due to the changed heat dissipation. After about the 5th layer, the $t_{12/8}$ time stabilizes at a certain level that depends on the arc energy.
- 3 The ferrite content tends to decrease with increasing arc energy. At high arc energies, the filler metals optimized for joint welding can result in unacceptably high austenite contents. However, an approximate prediction of the FN can be made on the basis of the WRC-1992 diagram if the final chemical composition of the WAAM walls is known with sufficient accuracy, considering pickups and burning losses of alloying elements.
- 4 In addition to unacceptable ferrite-austenite ratios, undesirable phase precipitations can also occur. Among the tested filler metal compositions, secondary austenite and partly also nitrides are to be expected in particular. Other detrimental phase precipitations were not found.
- 5 The corrosion tests carried out in accordance with the requirements of ISO 17781 and ASTM G48, Method A did not show any degradation of the corrosion resistance under the required test conditions.
- 6 The results of the superduplex wires of the type G Z 25 10 4 L and G Z 2 9 8 2 L indicate a potential suitability for WAAM due to the achieved ferrite-austenite ratio and the extensive absence of secondary austenite. In the case of standard duplex wires, an adjustment of the alloy composition seems to be necessary to reduce the risk of γ_2 formation on the one hand and to enable a balanced ferrite-austenite ratio over a wide range of arc energies on the other hand. The authors recommend the testing of an adapted alloying concept based on the G 22 9 3 N L with the nominal composition: Cr \approx 23.0 %, Ni \approx 7.5 %, Mo \approx 3.1 %, Mn \approx 1.6 %, Si \leq 0.4 %, Cu \leq 0.1 %, W \leq 0.01 %, N \approx 0.16 % (values in wt.%).

Acknowledgments Open Access funding enabled and organized by Projekt DEAL. The present contribution is a part of the AiF project IGF-No. 20.361B/DVS-No. 01.3060 of the German Research Association on Welding and Allied Processes (DVS). It was kindly supported by the AiF (German Federation of Industrial Research Associations) within the program for promoting the Industrial Collective Research (IGF) of the Federal Ministry for Economic Affairs and Energy (BMWi), based on a decision by the German Bundestag. Sincere thanks are given for this support and to the representing companies actively involved in the project committee.

Open Access This article is licensed under a Creative Commons Attribution 4.0 International License, which permits use, sharing, adaptation, distribution and reproduction in any medium or format, as long as you give appropriate credit to the original author(s) and the source, provide a link to the Creative Commons licence, and indicate if changes were

made. The images or other third party material in this article are included in the article's Creative Commons licence, unless indicated otherwise in a credit line to the material. If material is not included in the article's Creative Commons licence and your intended use is not permitted by statutory regulation or exceeds the permitted use, you will need to obtain permission directly from the copyright holder. To view a copy of this licence, visit <http://creativecommons.org/licenses/by/4.0/>.

References

- Allen J (2006) An investigation into the comparative costs of additive manufacture vs. machine from solid for aero engine parts. *Cost Effective Manufacture via Net-Shape Processing*: 17–1–17–10.
- Gebhardt A (2013) *Generative Fertigungsverfahren [Generative manufacturing processes]*. Carl Hanser Verlag, München
- Lachmayer R, Lippert RB, Fahlbusch T (2016) 3D-Druck beleuchtet [3D printing illuminated]. Springer Vieweg, Berlin Heidelberg. <https://doi.org/10.1007/978-3-662-49056-3>
- Ding J, Colegrove P, Mehnen J, Ganguly S, Sequeira Almeida PM, Wang F, Williams S (2011) Thermo-mechanical analysis of wire and arc additive layer manufacturing process on large multi-layer parts. *Comput Mater Sci* 50:3315–3322. <https://doi.org/10.1016/j.commatsci.2011.06.023>
- Colegrove PA, Coules HE, Fairman J, Martina F, Kashoob T, Mamash H, Cozzolino LD (2013) Microstructure and residual stress improvement in wire and arc additively manufactured parts through high-pressure rolling. *J Mater Process Technol* 213:1782–1791. <https://doi.org/10.1016/j.jmatprotec.2013.04.012>
- Messer B, Oprea V, Wright A (2007) Duplex stainless steel welding: best practices. *Stainless Steel World*. Fluor Canada Ltd., Canada, pp 53–63
- Karlsson L (2012) Welding duplex stainless steels — a review of current recommendations. *Weld World* 56:65–76. <https://doi.org/10.1007/BF03321351>
- Posch G, Chladil K, Chladil H (2017) Material properties of CMT — metal additive manufactured duplex stainless steel blade-like geometries. *Weld World* 61:873–882. <https://doi.org/10.1007/s40194-017-0474-5>
- Hoefler K, Haelsig A, Mayr P (2018) Arc-based additive manufacturing of steel components—comparison of wire- and powder-based variants. *Weld World* 62:243–247. <https://doi.org/10.1007/s40194-017-0527-9>
- Stützer J, Zinke M, Jüttner S, Findekle P (2018) Additive Fertigung von Bauteilen aus Duplexstahl durch Schutzgasschweißen [Additive manufacturing of components made of duplex stainless steel by gas shielded arc welding]. *Proceedings of the DGM-Conference: Materials and Additive Manufacturing*: 103–108.
- Kotecki DJ, Siewert TA (1992) WRC-1992 constitution diagram for stainless steel weld metals: a modification of the WRC-1988 diagram. *Weld J* 71:171–178
- Stützer J, Zinke M, Jüttner S (2017) Studies on the pore formation in super duplex stainless steel welds. *Weld World* 61:351–359. <https://doi.org/10.1007/s40194-016-0409-6>
- ASTM G48-11 (2015) Standard test methods for pitting and crevice corrosion resistance of stainless steels and related alloys by use of ferric chloride solution. ASTM International, West Conshohocken
- ISO 17781 (2017) Petroleum, petrochemical and natural gas industries – test methods for quality control of microstructure of ferritic/austenitic (duplex) stainless steels. Beuth, Berlin
- Hosseini VA, Karlsson L, Engelberg D, Wessman S (2018) Time-temperature-precipitation and property diagrams for super duplex stainless steel weld metals. *Weld World* 62:517–533. <https://doi.org/10.1007/s40194-018-0548-z>
- Lippold JC, Kotecki DJ (2005) *Welding metallurgy and weldability of stainless steels*. John Wiley & Sons, Inc., Hoboken
- Knyazeva M, Pohl M (2013) Duplex steels. Part II: carbides and nitrides. *Metallogr Microstruct Anal* 2:343–351. <https://doi.org/10.1007/s13632-013-0088-2>
- Nilsson J-O, Karlsson L, Andersson J-O (1995) Secondary austenite formation and its relation to pitting corrosion in duplex stainless steel weld metal. *Mater Sci Technol* 11:276–283. <https://doi.org/10.1179/mst.1995.11.3.276>
- Ramirez AJ, Brandi SD, Lippold JC (2004) Secondary austenite and chromium nitride precipitation in simulated heat affected zones of duplex stainless steels. *Sci Technol Weld Join* 9:301–313. <https://doi.org/10.1179/136217104225021715>
- Nilsson JO, Wilson A (1993) Influence of isothermal phase transformations on toughness and pitting corrosion of super duplex stainless steel SAF 2507. *Mater Sci Technol* 9:545–554. <https://doi.org/10.1179/mst.1993.9.7.545>

Publisher's note Springer Nature remains neutral with regard to jurisdictional claims in published maps and institutional affiliations.